applied sciences

MDPI

Article

Prediction of Landslide Deformation Region Based on the Improved S-Growth Curve Model

Yuyang Li [1], Wen Nie [1,2,*], Qihang Li [3], Yang Zhu [4], Canming Yuan [1], Bibo Dai [2] and Qiuping Kong [5]

[1] School of Resources and Environmental Engineering, Jiangxi University of Science and Technology, Ganzhou 341000, China
[2] State Key Laboratory of Safety and Health for Metal Mines, Maanshan 243000, China
[3] School of Resources and Safety Engineering, Chongqing University, Chongqing 400044, China
[4] School of Mathematics and Physics, Lanzhou Jiaotong University, Lanzhou 730070, China
[5] Fujian Yonking Geotechnical Co., Ltd., Longyan 361000, China
* Correspondence: wen.nie@vip.tom.com

Abstract: Quantitative research on and the prediction of a landslide deformation area is an important point to accurately and comprehensively understand the failure mechanism of landslides and the degree of slope failure. This study uses image processing techniques to quantitatively identify the area and volume of deformation regions during rainfall-type landslide destabilization under multifactor conditions. The findings revealed that (1) an increase in rainfall intensity and slope angle, as well as the existence of slope crest, will accelerate the process of slope instability. In our study, when the rainfall intensity was 140 mm/h and the landslide volume reached 35.68%, the landslide failure was the most serious. (2) Slopes with high compaction of subsoil as well as those without perimeter pressure are relatively more damaged. (3) The higher the density of vegetation cover, the stronger the protection ability of the slope, and the higher the wind speed, the greater the failure to the slope. Furthermore, an improved S-growth curve model was proposed to predict landslide volumes in 16 sets of experiments. In detail, the proposed S-growth curve model predicted landslide volumes with an average absolute percentage error of 4.34–16.77%. Compared with the time series analysis moving-average method (average absolute percentage error of 6.39–68.89%), the S-growth curve model not only has higher prediction accuracy but also can describe the three stages of deformation region development from a physical perspective and can be applied to the volume during landslide change prediction.

Keywords: deformation area; landslide volume; type of space damage; S-growth curve model

Citation: Li, Y.; Nie, W.; Li, Q.; Zhu, Y.; Yuan, C.; Dai, B.; Kong, Q. Prediction of Landslide Deformation Region Based on the Improved S-Growth Curve Model. *Appl. Sci.* **2023**, *13*, 3555. https://doi.org/10.3390/app13063555

Academic Editor: Itzhak Katra

Received: 9 February 2023
Revised: 25 February 2023
Accepted: 2 March 2023
Published: 10 March 2023

1. Introduction

China has many mountainous areas, complex terrain, and structural development, and the frequent occurrence of severe weather, such as heavy rainfall, makes the number of casualties and economic losses caused by geological disasters, such as landslides, collapses, debris flows, and ground subsidence, higher in the world [1–3]. According to the National Geological Hazard Bulletin issued by the Ministry of Natural Resources of the People's Republic of China, the number of landslide disasters (54,257) accounted for nearly 71% of the total number of geological disasters (76,845) between 2012 and 2019 [4,5]. Rainfall is one of the main factors inducing landslides; influenced by the southeast monsoon and southwest monsoon climate, rainfall in most areas of China is mainly concentrated in May-September, and the number of geological disasters occurring in August-September is higher. Due to the influence of geographical conditions, landslides occur mainly in the central and southern and southwest and east of China [6–8]. The number and scope of landslides are large, and it is almost impossible to rely on protective measures, such as retaining walls and antislip piles, to prevent and control all slopes with potential landslide threats. Therefore,

it is of great significance to understand the occurrence mechanism of rainfall landslides and make effective early warning models and forecasting techniques [9,10].

Landslide model experiments are one of the important tools to study the evolutionary mechanism of landslides [11,12]. As early as the 1870s, researchers in the United States and Japan conducted research on rainfall-type landslide model experiments. Three sets of indoor physical model experiments were designed with selected landslide site materials, and the induced mechanism of loess landslides was revealed by combining experimental phenomena with data recorded by three sensors: a volumetric water content sensor, matrix suction sensor, and pore water pressure sensor [13]. Tan et al. concluded from the field model experiments that the main basis of deformation and damage of granite fully weathered soil slopes is the steep increase of water content and pore water pressure fluctuation; the instability is caused by the decrease of soil matrix suction due to rainfall infiltration, and thus the strength is reduced; itsdamage mode is local slope slip followed by cracks, and finally, large-scale collapse [14]. Yang et al. conducted experiments on landslide models under the coupling effect of earthquakes and rainfall and found that after an earthquake, the superposition of adverse rainfall factors belonged to the typical disaster chain effect with an obvious crack development in the middle and rear of the model and a large deformation at the leading edge of the slope [15]. The study on the landslide mechanism provides a theoretical basis for landslide early warning forecasting. Based on the negative correlation between the deformation velocity time-series curve and slope stability, Qin et al. established a landslide damage time prediction model with rapid convergence of slope stability [16]. Currently, landslide early warning and forecasting methods still mainly rely on slope surface displacement detection. By conducting indoor model experiments on specific research areas and summarizing and analyzing the results of indoor model experiments as well as field displacement detection data, the relationship between displacement rate and duration in the accelerated deformation stage of slopes was established, and finally, the prediction method of landslide damage time was proposed. Xu Qiang's team conducted a detailed study on the formation mechanism of the Hefangtai loess landslide in Gansu, constructed an early warning model to cope with sudden-type loess landslides based on its damage characteristics, and successfully predicted the time of landslide occurrence [17–19].

Although the landslide failure time prediction method has been successfully applied in some indoor and field cases, it has certain drawbacks because it relies on the displacement data measured by contact sensors. First of all, the displacement sensor hardware cost is high, the installation is complicated, the maintenance is difficult, and the staff during the construction process has a certain danger; secondly, there are high requirements for the buried position of the sensor, and improper positioning of the sensor will seriously affect the accuracy of prediction; finally, the information obtained by the sensor is very limited, the information collected has a large amount of noise, and the displacement sensor can only reflect a small change, which is difficult to reflect the overall situation of the slope. Considering the above problems in displacement monitoring, noncontact monitoring methods have begun to attract the attention of some scholars because of their advantages of convenient installation and simple maintenance. Some scholars have realized the automatic identification of a landslide deformation area through landslide images collected with noncontact monitoring equipment [20,21], for example, a method based on a combination of RGB color space and a support vector machine (SVM) to identify landslide areas [22]. The identified landslide area and volume play a very important role in understanding the slope damage degree and evaluating remedial methods [23–25]. However, there are relatively few studies on the change law of landslide area and volume during the landslide instability process.

This paper collects the data from indoor rainfall model tests completed by the team in recent years [26–28]. These experiments used the control variable method to study the instability and failure of rain-type slopes under different experimental conditions (rainfall intensity, slope angle, presence or absence of slope crest, base soil compaction, presence

or absence of confining pressure, vegetation cover density, and wind level). The main purpose is to quantitatively identify the failure area and volume in the whole process of slope instability, to study its change pattern under different experimental conditions, to find the commonalities and differences in the slope instability process based on experimental phenomena, and to reveal the evolution mechanism of rainfall-type landslides. Meanwhile, an improved S-growth curve model is proposed to predict landslide volume using the value of landslide volume at two moments with an interval of 5 min and the factors affecting the landslide volume as the input values. The research results can provide a scientific basis and theoretical support for landslide risk assessment and early warning prediction methods.

2. Physics Experiments

2.1. Experimental System

The physical experiment system is mainly composed of a model box, a rainfall device, a monitoring device, and a computer. The model box and rainfall device form the rainfall system. In Figure 1a, the length, width, and height of the model box are 1.6 m × 0.8 m × 0.8 m, the volume is 1.024 m^3, and 8–13 are the details of the rainfall device which contains a total of 15 fogging nozzles and 5 flow meters, and the flow meter is used to control the rainfall intensity. The monitoring device is a trinocular camera (Figure 1b) (type: Point Grey Bumblebee × 3, resolution: 1280 × 960), and the slope change pattern during the whole process of the experiment was monitored, and its placement position was 1.2 m from the ground and 1.5 m from the landslide surface. The collection and processing of experimental data were done by computer.

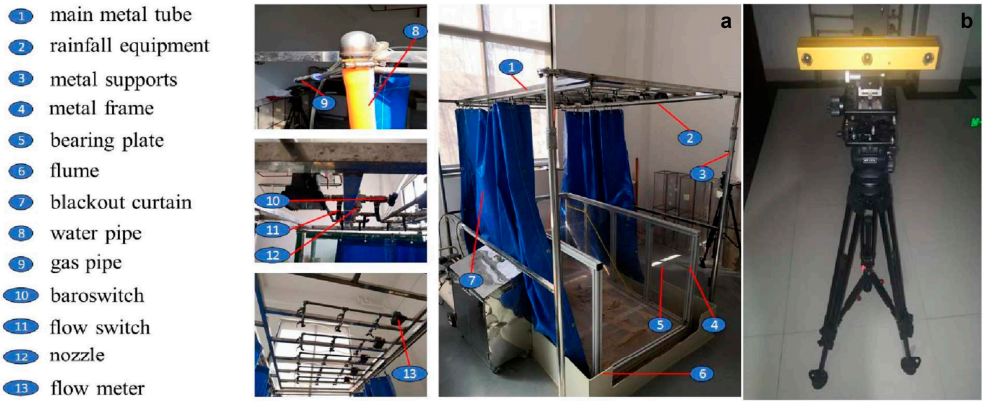

Figure 1. Physical experiment system. (**a**) Rainfall system and (**b**) trinocular stereo camera.

2.2. Experimental Program

The background of the model experiment is the coastal slope of Fujian Province, China, which has a subtropical monsoon climate and has long been under the influence of low-latitude tropical cyclones with frequent typhoons and rainstorm disasters. Typhoon season mainly occurs from July to September, and typhoons often cause heavy to very heavy rainfall in eastern Fujian, with the highest frequency and magnitude of heavy rainfall occurring in eastern Fujian due to typhoons crossing Taiwan Island. The relationship between typhoon intensity and rainfall at the rainstorm center generally shows a trend that the greater the wind speed at the time of landing, the greater the rainfall at the maximum rainstorm center, but the two are not closely related. The wind is strong in the coastal area in autumn and winter and small in spring and summer, and the average wind speed increases significantly from mid to late September. In winter, it is often influenced by the topographic trough of Taiwan, and the pressure gradient in the Taiwan Strait and the coastal areas of Fujian is very large, and the average wind speed also reaches the maximum of the year, such as the average wind speed in Pingtan and Chongwu are more than 6.7 m/s, but the wind speed is greatly influenced by the topography, and the wind speed in Ningde in the same period in the harbor is only below 1.2 m/s.

As shown in Table 1 below, the experiments of four working conditions were conducted according to the different factors influencing the study of rainfall-type landslides, containing a total of 16 sets of experiments. The experiment used the controlled variable method to investigate the destabilization damage of rainfall-type landslides under different experimental conditions by strictly controlling other experimental conditions when studying a certain factor. For Working Condition 1, this study was carried out mainly from three perspectives of rainfall intensity, slope angle, and the presence or absence of slope top platform, and the experimental material was sandy soil of a coastal slope with 3% water content. For Working Condition 2, the deformation damage of two different subgrade soil compaction degrees under the same rainfall conditions was mainly studied. The thickness of the experimental surface soil was 15 cm, the dry density was 1.12 g/m^3, and the compaction was 65.2%, and the thickness of the subgrade soil was 50 cm, and the compaction was 75.71% and 81.54%. The corresponding dry density of the soil was 1.3 g/m^3 and 1.4 g/m^3, respectively. For Working Condition 3, the influence of the presence or absence of the enclosing pressure on both sides of the slope on its stability was studied. The loading of the enclosing pressure was performed by laying a film of polymer material that could be inflated around the slope model and using a hydraulic device to inflate and pressurize the film to simulate the lateral pressure, and the material used in the experiment was fine sand with 13% water content. The quantitative analysis of the rainfall intensity and the applied enclosing pressure was not carried out in the two groups of experiments, and it was only required that the rainfall intensity agreed and that the size of the enclosing pressure was appropriate. For Working Condition 4, this study was carried out from two perspectives: the density of vegetation cover and the magnitude of wind speed. The vegetation cover density was divided into low-density vegetation, normal density vegetation, and high-density vegetation, and they were mainly distinguished by the number of vegetation they contained under the same canopy cover. According to the vegetation species, vegetation distribution, and the size of the main vegetation in the study area, small shrubs with an average height of about 20 cm and a maximum length of about 5 cm in the horizontal direction and 4 cm in the depth direction of the roots were selected as the vegetation used in the experiment, and the vegetation canopy coverage was about 65%. The wind speed model was selected from Typhoon Meranti in 2016, which had a landfall wind speed rating of 15 and a wind speed rating range of 12~13 when it crossed the study area with an impact time of 4~5 h and a rainfall intensity of 300 mm/d, bringing 2~3 d of heavy rainfall to the study area.

Table 1. Physical model experiments.

Working Condition	Experimental Grouping	Experimental Variables						
		Rainfall Intensity	Slope Angle	Slope Crest	Compaction of Subsoil	With or Without Perimeter Pressure	Vegetation Cover Density	Wind Speed
1	S1	30 mm/h	45°	20 cm	/	/	/	/
	S2	65 mm/h	45°	20 cm	/	/	/	/
	S3	140 mm/h	45°	20 cm	/	/	/	/
	S4	65 mm/h	30°	20 cm	/	/	/	/
	S5	65 mm/h	60°	20 cm	/	/	/	/
	S6	65 mm/h	45°	None	/	/	/	/
2	S7	45 mm/h	30°	None	75.71%	/	/	/
	S8	45 mm/h	30°	None	81.54%	/	/	/
3	S9	/	45°	40 cm	/	Yes	/	/
	S10	/	45°	40 cm	/	No	/	/

Table 1. *Cont.*

Working Condition	Experimental Grouping	Experimental Variables						
		Rainfall Intensity	Slope Angle	Slope Crest	Compaction of Subsoil	With or Without Perimeter Pressure	Vegetation Cover Density	Wind Speed
4	S11	60 mm/h	30°	None	/	/	Low Density	/
	S12	60 mm/h	30°	None	/	/	General Density	/
	S13	60 mm/h	30°	None	/	/	High Density	/
	S14	60 mm/h	30°	None	/	/	/	0 m/s
	S15	60 mm/h	30°	None	/	/	/	5.6–5.8 m/s
	S16	60 mm/h	30°	None	/	/	/	7.3–7.6 m/s

3. Quantitative Analysis of Landslide Deformation Area

3.1. Quantitative Analysis Methods

Quantitative analysis of a landslide deformation region mainly refers to calculating the area and volume of the landslide during the period from the beginning to the end of instability, calculating the average rate of change of the landslide area and volume within 5 min time according to the obtained area and the volume of the landslide at each moment, and drawing the quantitative analysis curves of deformation area, which are the cumulative area percentage curve, cumulative volume percentage curve, area change rate curve, and volume change rate curve, respectively. The data used in this study are mainly images and point clouds containing depth information, which were accumulated from the model experiments completed by the subject group in recent years. The acquisition was conducted by a trinocular stereo camera that recorded the side slope every 3 s after the experiment started and then transmitted it to the computer for saving. These data investigate various factors affecting the stability of rainfall slopes, including the intrinsic configuration of the slope and external factors. The area and volume of slope damage were obtained by the software compiled by our group. The landslide identification software is shown in Figure 2. The main steps of the software operation are 2–8. Firstly, the angle of the slope, the image and point cloud at the moment of T_0, and the image and point cloud at the moment of T_n are input in order. Then, select the appropriate threshold value. Finally, click the calculation button to obtain the area and volume of slope damage at the moment of T_n.

To facilitate the comparison of experiments with different model sizes, the specific landslide area and landslide volume, as well as the rate of change of area and volume, were obtained and converted into percentage form. The area share and volume share of the landslide damage area are obtained by dividing the landslide area and volume by the total area of the slope surface and the total volume of the side slope, respectively. The principle of calculating the area and volume of the landslide is shown below.

Landslide area calculation: As shown in Figure 3a, the landslide image recorded by the trinocular camera is processed and recognized, the number of pixels contained in the fault area is identified, and the number of pixels in the landslide failure area is determined according to the actual area of the known slope and the total pixels contained in the slope to determine the percentage of the number of pixels in the landslide failure area to the total number of landslide pixels, and then the area of the landslide is calculated. The calculation formula is as follows (1):

$$S = S_0 \frac{n}{N} \quad (1)$$

where S is the landslide area, S_0 is the slope area, n is the number of pixels contained in the fault area, and N is the total number of pixels contained on the slope surface.

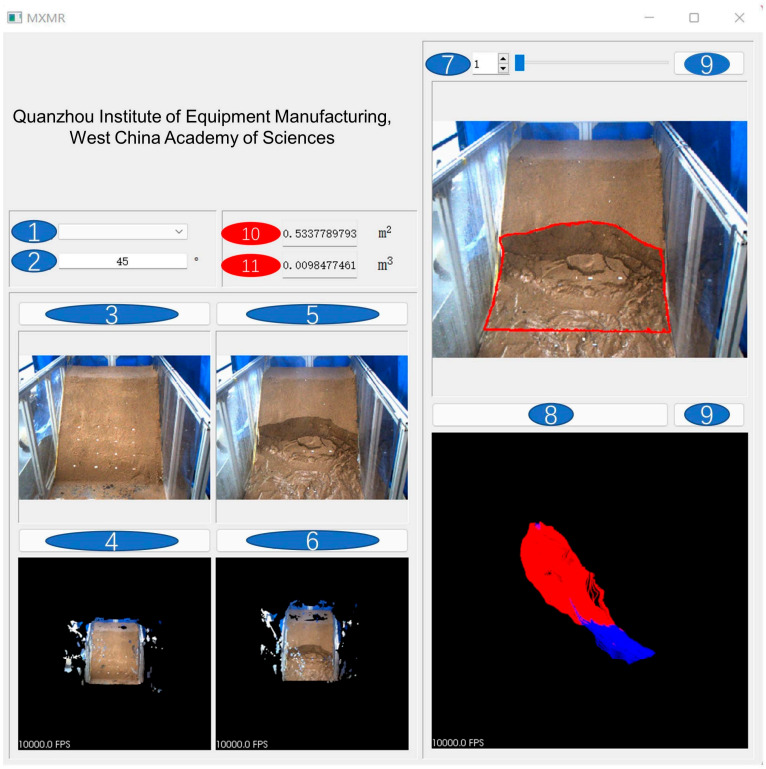

Figure 2. Landslide identification software. 1 Algorithm, 2 Slope angle, 3 Load T_0 moment image, 4 Load T_0 moment point cloud, 5 Load T_n moment image, 6 Load T_n moment point cloud, 7 Threshold, 8 Calculate, 9 Save, 10 Area, and 11 Volume.

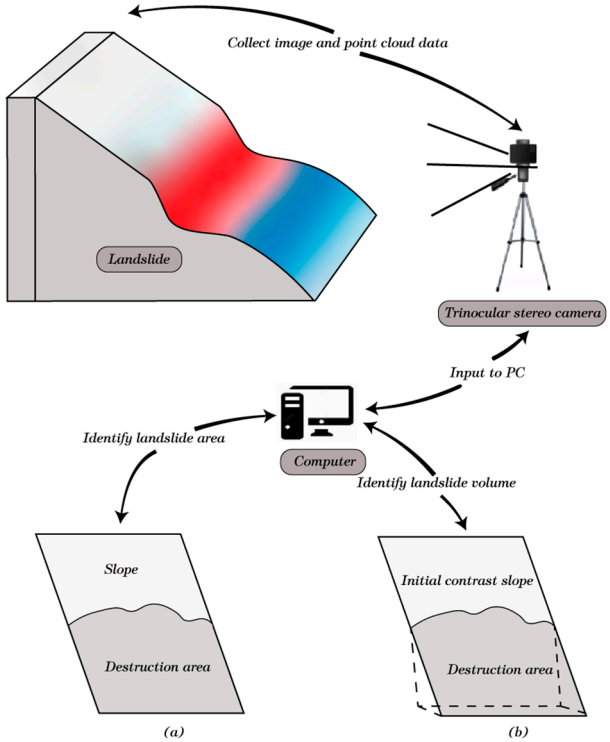

Figure 3. Schematic diagram of quantitative identification of deformation areas. (**a**) Schematic diagram of landslide area calculation. (**b**) Schematic diagram of landslide volume calculation.

Landslide volume calculation: The image recorded by the trinocular camera not only contains two-dimensional information on the slope surface but also records the

three-dimensional depth information of the slope, and the slope is reconstructed in three dimensions according to the Delaunay triangle network. As shown in Figure 3b, the surface of the slope before the experiment is set as the initial contrast surface, meshed into countless square grids of equal size, and the area of each grid is calculated according to the actual area of the slope. The slope surface at a selected moment is compared with the initial comparison slope surface for overlap, and the average depth difference between each mesh corresponding to the slope map and the initial comparison slope map at the selected time is calculated, respectively. The area with a mean difference greater than zero is a landslide depression area, the area with a mean difference less than zero is a slope protruding area, and the volume of the area with a mean difference in depth greater than zero is superimposed to be the volume of the slope failure area, as in Equation (2):

$$V = \sum_{0}^{n} h_n S_1 (h_n \geq 0) \quad (2)$$

Formula: V is the volume of the slope failure area, n is the number of meshes in the failure area, h_n is the average depth of the nth mesh, and S_1 is the area of each mesh.

When calculating the area and volume of slope failure area, there is a problem that the initial slope surface is not an ideal plane, the initial slope before the start of the experiment is set as the initial contrast breaking surface, and the calculated slope failure area and volume minus the initial comparative slope calculated failure area and volume is the real damage area and volume of the slope due to rainfall.

3.2. Experimental Results and Analysis

The damage areas of 16 groups of landslide experiments were quantitatively identified, and the quantitative analysis curves of landslide deformation areas were drawn, as shown in Figure 4. The longitudinal axis direction is divided into four parts, namely, a-cumulative area percentage curve, b-cumulative volume percentage curve, c-area rate of the change curve, and d-volume rate of the change curve. The horizontal axis direction is divided into seven parts, which are the seven influencing factors studied: (1) rainfall intensity (S1—30 mm/h, S2—65 mm/h, S3—140 mm/h), (2) slope angle (S4—30°, S2—45°, S5—60°), (3) slope crest (S2—20 cm, S6—none), (4) base soil compaction (S7—75.71%, S8—81.54%), (5) confining pressure (S9—yes, S10—none), (6) vegetation cover density (S11—low density, S12—general density, S13—high density), and (7) typhoons (S14—none, S15—typhoon, S16—strong typhoon). Table 2 summarizes the characteristic points of 16 groups of landslide experimental failures, which are the time point of landslide onset, the time point when the damage tends to stabilize, the maximum value of area and volume after the failure tends to stabilize, and the peak value of area and volume change rate.

Table 2. Experimental damage characteristic points.

Experiment	Start of Damage Time (min)	Damage Tendency Time (min)	Area Maximum (%)	Volume Maximum (%)	Peak Area Change Rate (%/min)	Peak Volumetric Rate of Change (%/min)
S1	92.5	112.5	97.42	11.13	16.15	2
S2	37.5	72.5	99.97	12.93	15.14	2.25
S3	2.5	37.5	99.99	35.68	19.99	3.71
S4	27.5	97.5	41.58	5.76	1.32	0.26
S5	17.5	77.5	99.98	8.53	17.81	0.58
S6	37.5	107.5	22.41	3.81	1	0.13
S7	27.5	62.5	63.57	9.79	2.87	0.62
S8	32.5	82.5	82.68	25.35	15.48	1.53
S9	7.5	57.5	59.83	2.16	4.53	0.1
S10	12.5	67.5	72.02	6.22	3.89	0.32
S11	37.5	132.5	26.55	9.23	1.08	0.29
S12	52.5	122.5	22.78	7.37	0.66	0.14
S13	77.5	122.5	20.43	5.77	0.55	0.16
S14	52.5	112.5	23.81	7.88	0.62	0.15
S15	42.5	122.5	29.12	10.7	0.69	0.21
S16	32.5	117.5	30.09	12.48	0.83	0.33

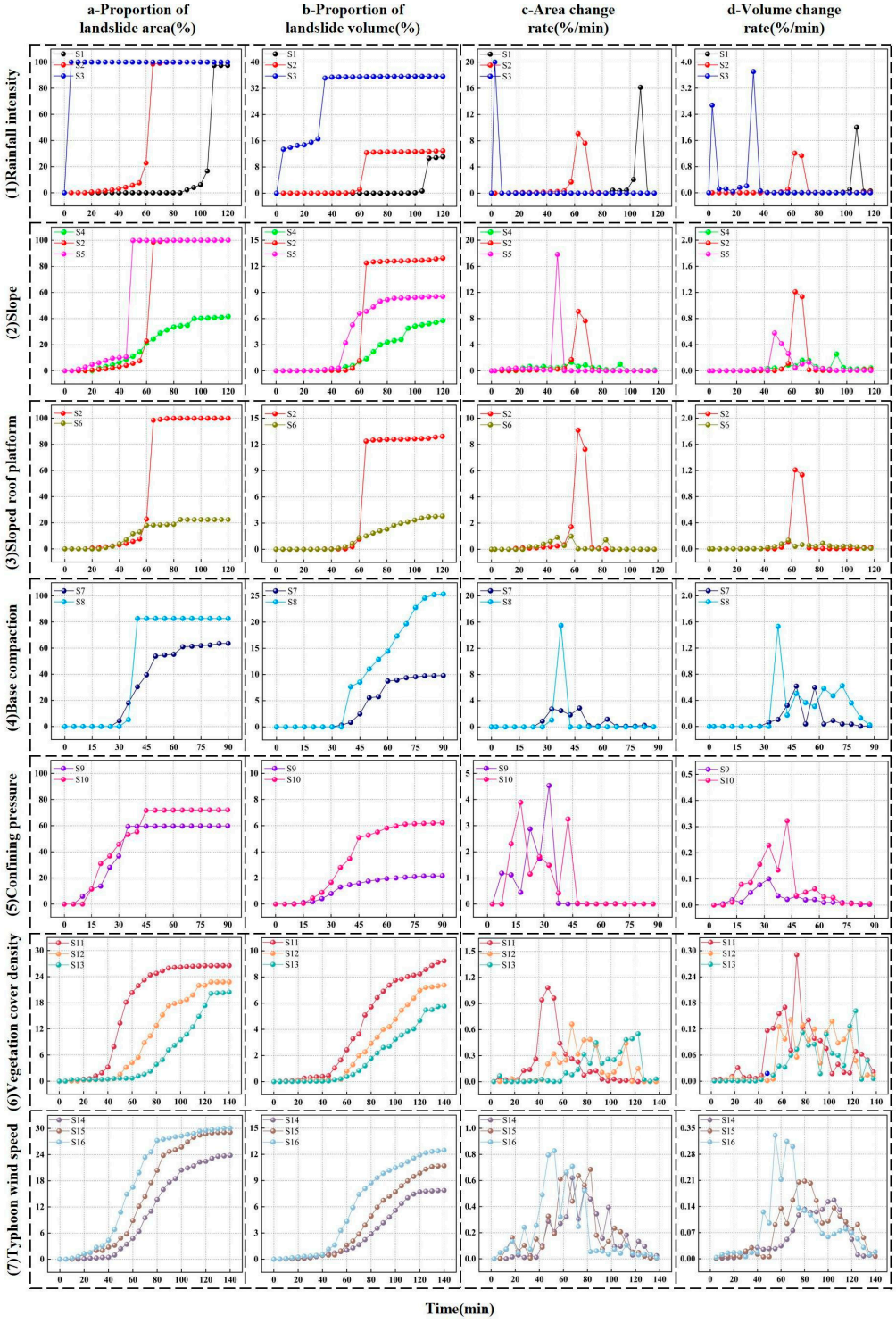

Figure 4. Quantitative identification curves of landslide: (**a**) represents the cumulative area percentage curve, (**b**) represents the cumulative volume percentage curve, (**c**) represents the area change rate curve, and (**d**) represents the volume change rate curve.

In Figure 4 (1), the greater the intensity of rainfall, the sooner the slope undermines and stabilizes. After the slope became stable, the slope surface of the three groups of experiments was completely destroyed, resulting in the landslide area accounting for nearly 100%, but the proportion of landslide volume after stabilization was different. After the shallow damage of the slope, the higher rainfall intensity made the slope go deeper to the direction of destruction, and the secondary damage occurred on the slope under the

action of 140 mm/h rainfall intensity, and the landslide volume accounted for the highest proportion in all experiments, reaching 35.68%. The instability mode of the progressive failure led to a single peak except for the double peak curve of the volume rate of change corresponding to the 140 mm/h rainfall intensity.

In Figure 4 (2), the larger the foot of the slope, the earlier the slope would be damaged on a larger scale. The 60° slope also collapsed, and its final damage area was close to 100%. Among the three different slope angle slopes, the 45° slope finally had the largest failure volume, and 30° was the smallest. The 30° landslide was a progressive receding failure, and the corresponding area change rate and volume change rate had multiple small peaks.

In Figure 4 (3), the landslide area and volume of the slope roof platform are much larger than those without the slope crest, which is also echoed by the landslide area change rate and volume change rate, indicating that the existence of the slope crest will seriously affect the stability of the slope.

In Figure 4 (4,5), 75.71% of the compaction degree of the base soil corresponds to the situation of confining pressure. Lower base soil compaction makes it easier for rainwater to infiltrate the base layer than higher soil compaction, resulting in relatively low water content in the shallow layer of the slope. On slopes with confining pressure, the pores between soil particles are small, rainwater infiltration is relatively difficult, and the soil water content is relatively small. Therefore, the degree of compaction of 81.54% of the base soil and the degree of damage of the slope without entrapment pressure is greater.

In Figure 4 (6), the slope covered with low-density vegetation was the first large-scale destruction followed by the slope covered with general density vegetation, and finally, the slope covered with high-density vegetation, and the order of slope failure tended to be stable. Vegetation has a certain interception effect on rainfall, prevents the topsoil from being washed and eroded by rainwater, indirectly prolongs the time of slope failure, and the vegetation root system and topsoil interact to form a root–soil complex, which increases the shear strength of the slope, inhibits the development and damage of the slope, and reduces the final damage degree of landslide. The above three sets of experiments with different vegetation coverage obviously proved that slope stability is related to vegetation cover density; under the action of simple rainfall, different vegetation cover densities have different degrees of reinforcement on the slope, and the higher the vegetation cover density, the more obvious the effect of preventing landslides. Comparing the time points of large-scale destruction of area and volume, it can be seen that the volume change lags behind the area change to varying degrees in the time dimension.

In Figure 4 (7), the slope damage degree is the greatest under the action of strong typhoon rain followed by typhoon rain, and the slope damage under the action of heavy rain is the smallest, which also proves that typhoons promote instability and damage of the slope, and the higher the wind level, the more likely the slope is to become unstable and the greater the degree of damage, which indirectly points out the limitations of vegetation protection in the presence of typhoons. It can be seen that experimental S11–S16 has an obvious initial failure stage, acceleration stage, and negative acceleration stage, and the change rate curve has multiple peaks, which belongs to the typical progressive retrogression failure. In summary, the degree of slope damage is strongly correlated with the seven influencing factors of the above study.

According to the process of multiple groups of experimental damage, it can be found that there are some common points and differences in the process of destabilization damage of rainfall-type landslides. The similarities are as follows: the destabilization damage of the slope starts from the foot of the slope and the surface of the slope; the landslide goes through three stages from the beginning to the end, occurrence, development, and maturity stage; throughout the process of slope instability damage, landslide area changes precede volume stabilization to a certain degree of time; the essential reason of rainfall triggering the landslide, the infiltration of rainwater, on the one hand, leads to the softening of soil, and as the shear strength decreases, on the other hand, the water content of soil increases, the weight of soil itself increases, the sliding force increases, and when the down-sliding force is

greater than the antisliding force is, the landslide will be produced. The difference is mainly reflected in that the failure process of the slope is different under different experimental conditions; the area, volume, failure speed, and time of landslide tending to be stable are different; and the failure mode of the slope is also different, which is generally divided into two types: push type and progressive pushback type.

4. Landslide Volume Prediction Model

4.1. S-Growth Curve

Many things in nature always go through three stages of occurrence, development, and maturity, and the change and development curve obtained according to the development law of these three stages is defined as an S-shaped growth curve. In the occurrence stage, things change more slowly; when it comes to the development stage, the speed of change accelerates, and things grow rapidly; finally, at maturity, the rate of change slows down until it is close to zero growth, and things hardly change. At present, S-curves have been widely used to describe and predict the development of individual growth, the development of organisms, and the development of certain technical and economic characteristics [29–32].

The S-growth curve (logistic function) model can be expressed as:

$$y = \frac{K}{1 + be^{-ax}},\ a > 0,\ b > 0,\ K > 0 \quad (3)$$

In Equation (3), x is the input variable, y is the output object, a and b are the parameters that determine the trend of the curve, and K is the environmental capacity. In the experiments we conducted, erosion began to occur when the cumulative rainfall (x) reached a certain threshold [33]. In the first phase, the landslide area and volume (y) grew slowly even with a certain time lag, especially in the case of low rainfall intensity and slope, high-density vegetation cover, and no typhoon action. Under the action of continuous rainfall, the slope failure entered the second stage, and the landslide area and volume increased rapidly. In the final stage, a new stable state was formed after the slope failure, and the rate of change of landslide area and volume began to decrease or even zero, and the landslide area and volume at this time were the environmental capacity (K).

4.2. S-Growth Curve Fitting

Three-dimensional landslide volume is used as the parameter that best reflects the damaged state of a slope. According to Equation (3), we fitted the volume change curves under 16 sets of experimental time series and found that the S-curve model matched the landslide volume development. As shown in Figure 5, the data in Figure 4 (b6,b7) are shown here as examples, where x is the cumulative rainfall, y is the landslide volume, K is the maximum landslide volume, and a and b are the parameters controlling the erosion rate. The mean absolute percentage errors (MAPE) of the fitted and observed values ranged from 12.4% to 91.7%. The parameters in the six models are given in Table 3.

Table 3. Fitting parameters.

Experiment	K	a	b
S11	8.75	328.72	0.0795
S12	7.7	373.62	0.0657
S13	6.34	350.56	0.0587
S14	8.35	499.75	0.0697
S15	10.77	359.61	0.0699
S16	11.89	262.91	0.0827

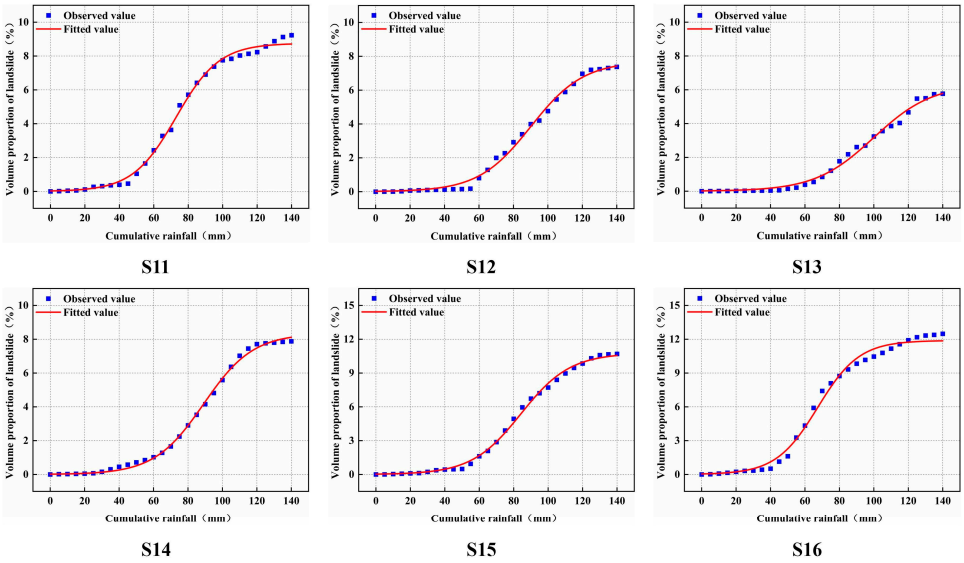

Figure 5. S-growth curve fitting (S11–S16).

4.3. Predictive Model Development

To predict (S-growth curve model) the landslide volume in the deformation zone, we used two consecutive observations (V_t, V_{t+1}) to train the parameters of the model so as to predict the landslide volume V_{t+2} at moment t + 2, and then repeated this process in the following time domain, which is similar to the dynamic update method. The landslide volume V_{t+2} at moment t + 2 was predicted using a modified S-shaped growth curve model as shown in Equation (4).

$$V_{t+2} = \frac{K'}{1 + b_t e^{-a_t(x_{t+2} - x_t)}},\ a_t > 0,\ b_t > 0, K' > 0 \tag{4}$$

where a_t and b_t are the parameters that affect the erosion rate at the time of t. x_{t+2} and x_t are the cumulative rainfall at time t + 2 and t.

Assuming that the cumulative rainfall x_t corresponding to the first observation selected is zero, according to the observations V_t and V_{t+1}, the value of b_t can be calculated by Equation (1) and then a_t can be calculated as follows:

$$b_t = \frac{K'}{V_t} - 1 \tag{5}$$

$$a_t = -\frac{\ln \frac{\frac{K'}{V_{t+1}} - 1}{b_t}}{x_{t+1} - x_t} \tag{6}$$

where K' is the environmental capacity, which here refers to the percentage of landslide volume after stabilization. As can be seen from the results in Table 2, K' has a linear relationship with the seven factors we examined, namely:

$$K' = \lambda i + \gamma \tag{7}$$

where i is the influence factor of the final damage volume of the landslide, and for experiments S11–S16, here, i refers to the vegetation cover density and typhoon wind speed, respectively. The coefficients λ and γ can be found by linear regression of the experimental data. Since the rainfall intensity was constant during the experiment according to the

assumption, then the cumulative rainfall $x_{t+2} = 2x_{t+1}$. After putting Equations (5)–(7) into Equation (4), the final model is as follows in Equation (8):

$$V_{t+2} = \frac{\lambda i + \gamma}{1 + \frac{\left(\frac{\lambda i+\gamma}{V_{t+1}} - 1\right)^2}{\frac{\lambda i+\gamma}{V_t} - 1}}, \; V_t > 0, \; \lambda i + \gamma\left(K'\right) > 0 \tag{8}$$

For the proposed model framework (8), we only need to input two the observation V_t at moment t, the observation V_{t+1} after 5 min, and the factor i that affects the environmental holding capacity to obtain the landslide volume percentage at moment t + 2. When new data for moments t + 1 and t + 2 are input, the model can predict the landslide volume percentage at moment t + 3. Here t, t + 1, t + 2, and t + 3 figuratively represent some moments. When we choose the time interval as 10 min, we can predict the landslide volume at the next 10 min by the two adjacent 10 min' volume values, and when we want to predict the landslide volume after a longer time, we only need to change the time interval between the two chosen values, and the prediction accuracy will decrease with the increase in time interval. Figure 6 shows the prediction results based on the improved S-shaped growth curve model for experiments S11–S16. The prediction results agree well with the observed values, and the average absolute percentage error ranges from 6.01% to 16.45%.

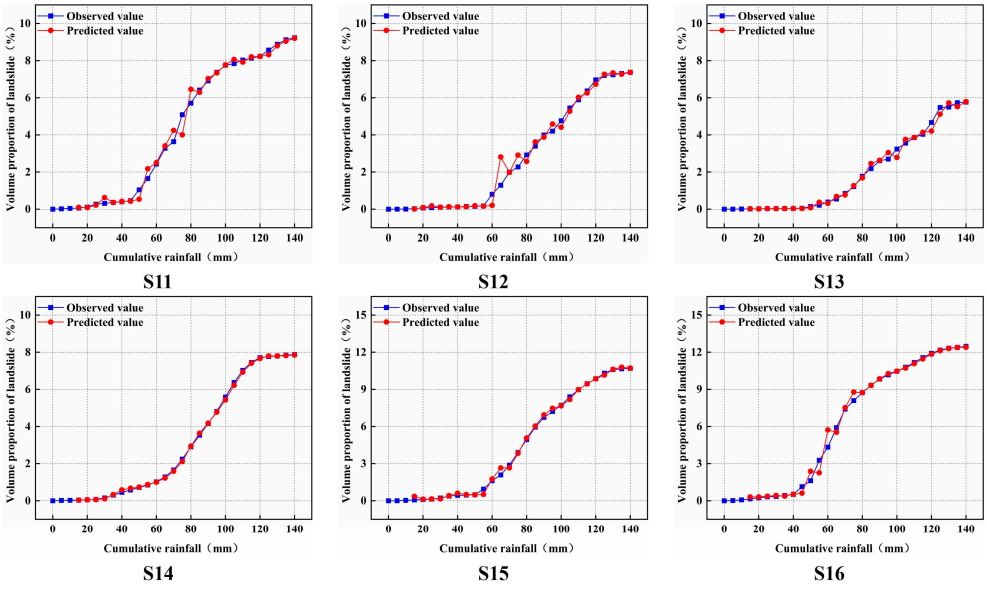

Figure 6. S-growth curve model prediction results (S11–S16).

5. Discussions

5.1. Evolutionary Pattern of Deformation Area

The evolution mechanism of a rainfall-type landslide is that, with the beginning of rainfall, part of the rainwater infiltrates into the body of the slope, and part of the rainwater collects together to form surface runoff and flows toward the foot of the slope; this process will carry away the unstable particles on the surface of the slope and cause shallow damage to the surface of the slope. As the rainfall continues, the soil body at the foot of the slope will first reach saturation, producing smaller damage and laying a hidden danger for the instability of the slope with the area and volume change curve showing a smaller value plus from zero to there. Under the infiltration of rainwater in the middle and upper part of the slope, the water content of the soil increases rapidly, the pore water pressure increases, the suction force of the matrix decreases, the interaction between the water body, and the internal material of the slope causes the internal structure to change, resulting in a reduction of its strength characteristics, and the capacity of the soil itself increases, indirectly leading to an increase of the sliding force of the slope; the slope becomes unstable and cracks

begin to appear. When the internal fracture of the slope is fully penetrated and a complete sliding surface is formed, the first sliding of the middle and low part of the slope provides space for larger sliding to occur in the upper part, which will subsequently produce larger sliding damage, which also corresponds to the peak of the area change rate and volume change rate.

The development of the deformation zone in the process of slope instability failure is mainly divided into three stages which can be called the preslip stage, the sliding failure stage, and the stabilization stage. The preslip stage refers to the interval from stability to near the appearance of damage on the slope; the performance of this stage is that the slope, under the action of rainfall, gradually increases in moisture content, increasing the slope's weight. The sliding force gradually increases close to the antislip force, and the landslide area and volume in this process have almost no value. The sliding failure phase refers to the interval between the beginning of the slope and the end of the failure. As shown in Figure 6, the slide failure stage divides the landslide into two types: progressive type and progressive backward type according to the type of spatial failure [34]. The spatial damage types of all experiments almost always fit these two patterns (Figure 7a). The progressive failure is manifested as follows: Under the action of a large sliding force, the trailing edge of the landslide first produces tensile cracks, and then the soil in the back section continues to develop forward and inside the slope, and the soil in the antislip section in front of the push is deformed, forming a rising crack on the leading edge; this type of landslide failure is faster, the landslide area and volume increase exponentially and then tend to be stable, and the landslide area and volume change rate curve have a large peak (Figure 7b). Progressive receding failure is manifested as follows: With continuous rainfall, a certain amount of water is formed at the foot of the slope, resulting in the first occurrence of a soil liquefaction phenomenon at the foot of the slope, resulting in collapse or slip deformation, forming a new empty surface, and the soil adjacent to the empty surface will result in slip deformation or partially collapse under the action of rainfall and so on until the slope finally reaches a stable state, and the landslide area proportion and volume ratio curve under this process time series belong to the step type. There are multiple peaks in the rate of area change and the rate of volume change. The stabilization stage is characterized by the end of the landslide and the slope in a new equilibrium and stable state, and the cumulative landslide area and volume of this stage hardly change, and the area change rate and volume change rate are close to zero.

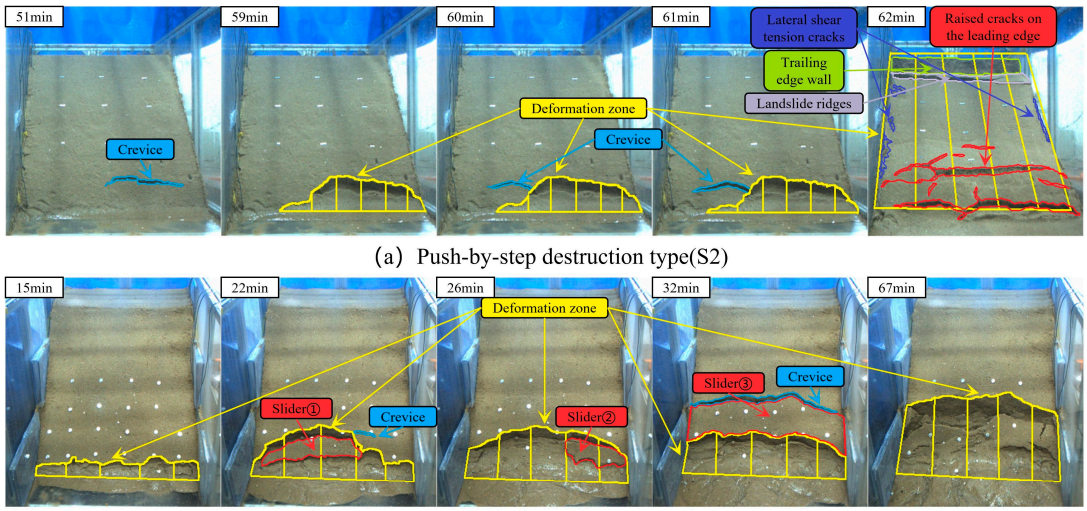

Figure 7. Types of spatial damage to landslides.

5.2. Comparison of the Improved S-Curve-Based Model with the Time Series Analysis Moving-Average Model

A simple time series analysis moving-average can be used to predict landslide volume [35,36]. Equation (9) uses the average of the landslide volume at three consecutive moments as the predicted value for the fourth moment.

$$V_t' = \frac{V_{t-1} + V_{t-2} + V_{t-3}}{3},\ t \geq 4 \tag{9}$$

where V_t' is the output object of the prediction model at time t. V_{t-1}, V_{t-2}, and V_{t-3} are the observed data at times $t-1$, $t-2$, and $t-3$, respectively. The volumes of the landslide deformation areas of experiments S1–S16 are predicted using Equations (8) and (9), respectively, and the predicted results are shown in Figure 8 (S11–S16) and Table 4 (S1–S16).

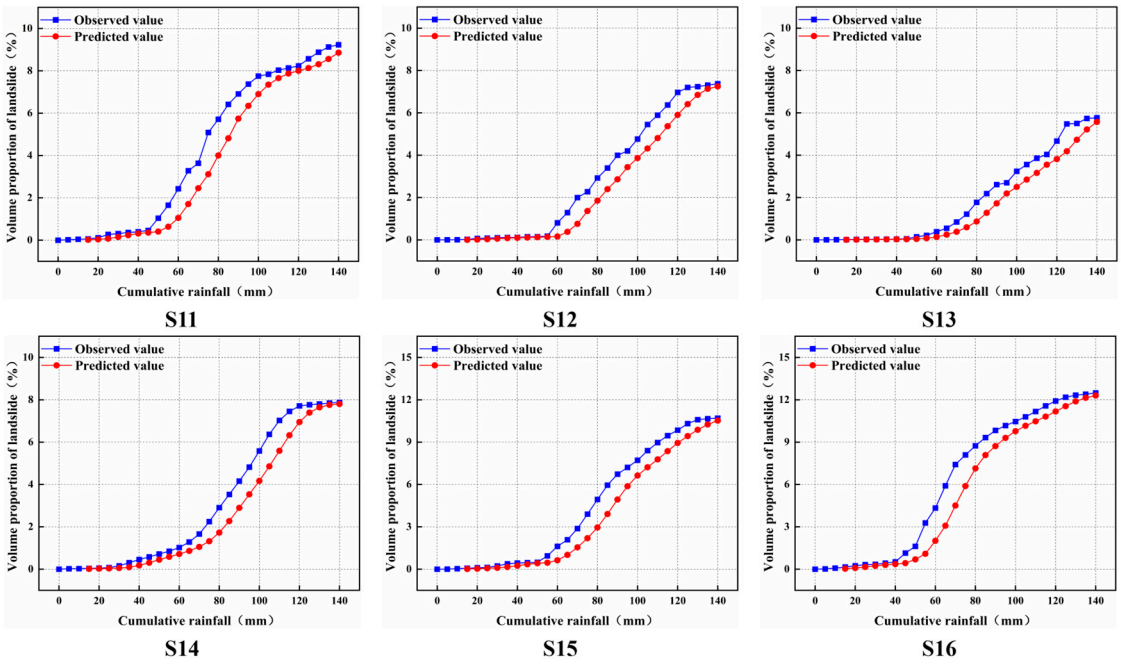

Figure 8. Moving average model prediction results (S11–S16).

Table 4. Landslide volume error (MAPE) predicted by S-growth curve model and moving average model.

Experiment	S-Growth Curve Model Prediction Error	Moving Average Model Prediction Error	Experiment	S-Growth Curve Model Prediction Error	Moving Average Model Prediction Error
S1	16.77%	68.89%	S9	5.57%	24.65%
S2	12.70%	30.73%	S10	4.34%	23.55%
S3	6.05%	6.39%	S11	12.21%	29.33%
S4	10.59%	37.94%	S12	16.45%	32.02%
S5	6.25%	30.62%	S13	13.57%	34.94%
S6	6.52%	35.00%	S14	6.01%	32.63%
S7	10.78%	31.30%	S15	10.98%	30.47%
S8	4.36%	24.00%	S16	10.83%	26.13%

First of all, it can be seen from Table 4 that the prediction result of the improved S-growth curve model is better than that of the moving average model. The S-curve prediction model contains information on the S-curve trend, so it can describe the whole process, especially the phase change. Secondly, the prediction of the moving average model

depends on the previous data, but it cannot simulate the sudden change from the presliding stage to the sliding failure stage. Therefore, the error always exists in the sliding failure stage. It is obvious from Figure 8 that all prediction results of the moving average model lag behind the observed values to a certain extent. Finally, the moving average model is similar to a "black box". Its use only involves input and output without any clear physical meaning or process. In our research, the S-shaped growth curve prediction model needs external influencing factors and a continuous landslide volume as parameters, and it can also describe the three stages of deformation zone growth from a physical point of view.

5.3. Highlights of this Study and Outlook

The highlight of this study is that through the quantitative identification of the deformation area of multiple sets of model tests, the evolution law of the deformation area of the whole failure stage of a slope was systematically studied, and the landslide volume was successfully predicted based on the improved S-shaped growth curve. In this experiment, various factors, such as rainfall intensity, slope angle, and slope morphology, were considered, while the existing experimental studies on landslide influencing factors were relatively single, and the evolution characteristics of deformation zones were rarely quantitatively studied. At present, noncontact monitoring equipment has been applied to real landslides (Nanping Highway slope in Fujian, China) [37]. We plan to focus on the evolution of the deformation zone from the prelandslide stage to the beginning of the rapid slide failure through indoor model experiments, strive to construct the relationship between landslide volume rate and duration, and propose a landslide failure time prediction method.

6. Conclusions

Based on the experimental data of multiple sets of indoor rainfall landslide models and combined with computer vision technology, the fault areas of each experimental slope were quantitatively identified, and the evolution of the deformation area of the landslide under different experimental conditions was studied. We also propose an S-curve model to predict landslide volume and effectively verified it through six physical experiments. These valuable conclusions include:

(1) Under continuous rainfall conditions, a certain amount of rainwater will first converge at the foot of the slope, causing the first damage to occur at the foot of the slope and then triggering larger-scale damage. In this process, the slope damage degree shows the trend of the S-growth curve, and the slope damage mode also shows two types of damage, namely, nudge damage and progressive backward push.

(2) The intensity of rainfall and landslide volume are negatively correlated. The larger the slope angle is, the faster the slope destabilization damage is, but the landslide volume value is the largest for the slope angle of 45°. The presence of a slope roof platform will accelerate the damage of the slope and increase the degree of damage. The soil compaction degree of the base layer is higher, and a slope without confining pressure will have a greater degree of damage. In the absence of wind, vegetation plays a certain protective role in the stability of the slope, and the greater the vegetation cover density, the more obvious the protective effect. In the case of wind, the vegetation on the damage of the slope plays a certain role in enhancing it, and the greater the wind speed, the more serious the slope damage.

(3) When a slope is washed by raindrops, and the surface runoff is formed by rainwater, the unstable particles on the surface of the slope will be carried away and then the direction of depth develops, as shown in the quantitative analysis curve of the deformation area above. The landslide volume change has a certain time lag relative to the area change, and the landslide volume continues to increase after the landslide area tends to be stable.

(4) Compared with the time series analysis moving-average model for predicting landslide volume change, the improved S-shaped growth curve model with two landslide

volumes at 5 min intervals and influencing factor (i) as an input can predict the change process of landslide damage degree more accurately.

Author Contributions: Data organization, statistical analysis, writing—original draft, Y.L.; software, investigation, supervision, Q.L.; conceptualization, methodology, Y.Z.; software, investigation, C.Y.; validation, formal analysis, B.D.; validation, Q.K.; funding acquisition, methodology, writing—review and editing, W.N. All authors have read and agreed to the published version of the manuscript.

Funding: This work was supported by Jiangxi Provincial Natural Science Foundation (No. 20212ACB214005) and the Major Science and Technology Projects of Anhui Province (No. 202003a0702002).

Institutional Review Board Statement: Not applicable.

Informed Consent Statement: Not applicable.

Data Availability Statement: Please contact the corresponding author when you need the data on the results of this study.

Conflicts of Interest: The authors declare that they have no known competing financial interests or personal relationships that could have appeared to influence the work reported in this paper.

References

1. He, S.; Wang, J.; Liu, S. Rainfall Event–Duration Thresholds for Landslide Occurrences in China. *Water* **2020**, *12*, 494. [CrossRef]
2. Lin, Q.; Wang, Y.; Liu, T.; Zhu, Y.; Sui, Q. The Vulnerability of People to Landslides: A Case Study on the Relationship between the Casualties and Volume of Landslides in China. *Int. J. Environ. Res. Public Health* **2017**, *14*, 212. [CrossRef] [PubMed]
3. Lin, Q.; Wang, Y. Spatial and temporal analysis of a fatal landslide inventory in China from 1950 to 2016. *Landslides* **2018**, *15*, 2357–2372. [CrossRef]
4. Ministry of Land and Resources of the People's Republic of China. *National Geological Disaster Bulletin 2012–2017*; Ministry of Land and Resources of the People's Republic of China: Beijing, China, 2017.
5. Ministry of Land and Resources of the People's Republic of China. *National Geological Disaster Bulletin 2018–2019*; Ministry of Land and Resources of the People's Republic of China: Beijing, China, 2019.
6. China Meteorological Administration. *China Climate Bulletin 1997–2018*; China Meteorological Administration: Beijing, China, 2018.
7. Liu, C.; Chen, C. Research on the origins of geological disasters in China. *Geol. Rev.* **2020**, *66*, 1334–1348. [CrossRef]
8. Liang, G.; Zhang, X.; Ling, X.; Zhou, H.; Lin, W. Analysis of Temporal-spatial Characteristics of Geological Disasters in China from 2009 to 2019. *J. Disaster Prev. Reduct.* **2021**, *37*, 58–64. [CrossRef]
9. Intrieri, E.; Gigli, G.; Mugnai, F.; Fanti, R.; Casagli, N. Design and implementation of a landslide early warning system. *Eng. Geol.* **2012**, *147–148*, 124–136. [CrossRef]
10. Uchimura, T.; Towhata, I.; Wang, L.; Nishie, S.; Yamaguchi, H.; Seko, I.; Qiao, J. Precaution and early warning of surface failure of slopes using tilt sensors. *Soils Found.* **2015**, *55*, 1086–1099. [CrossRef]
11. Alsubal, S.; Sapari, N.b.; Harahap, I.S.H.; Ali Mohammed Al-Bared, M. A review on mechanism of rainwater in triggering landslide. In *IOP Conference Series: Materials Science and Engineering*; IOP Publishing: Bristol, UK, 2019; Volume 513, p. 012009. [CrossRef]
12. Lou, X.; Liu, G.; Wu, J.; Cheng, S.; Shen, H.; Xu, K.; Huang, X. Model test study on landslide under rainfall and reservoir water fluctuation. *Chin. J. Rock Mech. Eng.* **2005**, *14*, 2476–2483.
13. Wang, G.; Xun, P.; Wu, L.; Shi, L.; Zhu, E. Experimental Study on Mechanism of Shallow Loess Landslides Induced by Rainfall. *J. Eng. Geol.* **2017**, *25*, 1252–1263. [CrossRef]
14. Tan, J.; Wu, H.; Wang, S.; Li, G. Field Model Test of Disaster Caused by Granite Completely Weathered Soil Slope under Heavy Rainfall. *Sci. Technol. Eng.* **2022**, *22*, 12307–12314. [CrossRef]
15. Yang, X.; Chen, K.; Diao, X.; Zhou, T. Model tests and stability of accumulation landslides under coupling action of earthquake and rainfall. *Chin. J. Geotech. Eng.* **2022**, *44*, 58–62. [CrossRef]
16. Qin, H.; Ma, H.; Yu, Z. Analysis Method of Landslide Early Warning and Prediction Supported by Ground-Based SAR Technology. *Geomat. Inf. Sci. Wuhan Univ.* **2020**, *11*, 1697–1706. [CrossRef]
17. Li, B.; Xu, Q.; Cheng, Q.; Liu, T.-X.; Tang, M.-G.; Zheng, G.; Wang, H.-Y. Characteristics of discontinuities in Heifangtai landslide area in Gansu, China. *Appl. Geophys.* **2021**, *17*, 857–869. [CrossRef]
18. Qi, X.; Zhu, X.; Xu, Q.; Zhao, K.; Huo, D.; Wang, H.; Xiu, D. Improvement and Application of Landslide Proximity Time Prediction Method Based on Saito Model. *J. Eng. Geol.* **2020**, *28*, 832–839. [CrossRef]
19. Fang, S.; Xu, Q.; Xiu, D.; Zhao, K.; Li, Z.; Pu, F. A study of the predicted instability time of sudden loess landslides based on the SLO model. *Hydrogeol. Eng. Geol.* **2021**, *48*, 169–179. [CrossRef]

20. Li, Q.; Song, D.; Yuan, C.; Nie, W. An image recognition method for the deformation area of open-pit rock slopes under variable rainfall. *Measurement* **2022**, *188*, 110544. [CrossRef]
21. Li, Q.; Geng, J.; Song, D.; Nie, W.; Saffari, P.; Liu, J. Automatic recognition of erosion area on the slope of tailings dam using region growing segmentation algorithm. *Arab. J. Geosci.* **2022**, *15*, 438. [CrossRef]
22. Wei, Z.; Wei, X. Landslide Recognition in Mountain Image Based on Support Vector Machine. *Meas. Technol. Mechatron. Autom. Electr. Eng.* **2012**, *135*, 279–286. [CrossRef]
23. Von Ruette, J.; Lehmann, P.; Or, D. Linking rainfall-induced landslides with predictions of debris flow runout distances. *Landslides* **2015**, *13*, 1097–1107. [CrossRef]
24. Leong, E.-C.; Cheng, Z. A geometry-modelling method to estimate landslide volume from source area. *Landslides* **2022**, *19*, 1971–1985. [CrossRef]
25. Yuan, C.; Nie, W.; Li, Q.; Geng, J.; Dai, B.; Gao, J. Automatic Batch Recognition of Rock Deformation Areas Based on Image Segmentation Methods. *Front. Earth Sci.* **2023**, *10*, 1093764. [CrossRef]
26. Song, S. Analysis of Artificial Rainfall Type Landslide Monitoring Based on Trinocular Vision Technology. Master's Thesis, Southwest Petroleum University, Chengdu, China, 2019.
27. Kang, S. Research on Response Characteristics of Slope Elastic Wave under Rainfall Conditions. Master's Thesis, Hebei University, Baoding, China, 2021.
28. Guo, Z. Three-Dimensional Stability Analysis of Slope Considering Rainfall Infiltration. Master's Thesis, Northwest A&F University, Xianyang, China, 2021.
29. Ram, Y.; Dellus-Gur, E.; Bibi, M.; Karkare, K.; Obolski, U.; Feldman, M.W.; Cooper, T.F.; Berman, J.; Hadany, L. Predicting microbial growth in a mixed culture from growth curve data. *Proc. Natl. Acad. Sci USA* **2019**, *116*, 14698–14707. [CrossRef] [PubMed]
30. Huang, F.; Zhang, M.; Li, Y.; Li, Z.; Fang, J.; Guo, K. The longitudinal trajectory of body mass index in the Chinese population: A latent growth curve analysis. *PLoS ONE* **2018**, *13*, e0207845. [CrossRef]
31. Xun, J.; Li, Z.; Su, W. Application of pearl model to the forecast of slope failure time. *Chin. J. Geol. Hazard Control.* **1993**, *02*, 38–43. [CrossRef]
32. Sovljanski, O.; Tomic, A.; Pezo, L.; Markov, S. Temperature and pH growth profile prediction of newly isolated bacterial strains from alkaline soils. *J. Sci. Food Agric.* **2020**, *100*, 1155–1163. [CrossRef]
33. Abu Mansor Maturidi, A.M.; Kasim, N.; Abu Taib, K.; Wan Azahar, W.N.A. Rainfall-Induced Landslide Thresholds Development by Considering Different Rainfall Parameters: A Review. *J. Ecol. Eng.* **2021**, *22*, 85–97. [CrossRef]
34. Li, X.; Li, Q.; Hu, Y.; Chen, Q.; Peng, J.; Xie, Y.; Wang, J. Study on Three-dimensional Dynamic Stability of Open-pit High Slope under Blasting Vibration. *Lithosphere* **2022**, *2022*, 6426550. [CrossRef]
35. Xu, Q.; Tang, M.; Xu, K.; Huang, X. Research on Space-Time Evolution Laws and Early Warning-Prediction of Landslides. *Chin. J. Rock Mech. Eng.* **2008**, *27*, 1104–1112.
36. Liu, C.; Huang, J.; Ji, F.; Zhang, L.; Liu, X.; Wei, Y.; Lian, X. Improvement of the global prediction system of the COVID-19 pandemic based on the ensemble empirical mode decomposition (EEMD) and autoregressive moving average (ARMA) model in a hybrid approach. *Atmos. Ocean. Sci. Lett.* **2021**, *14*, 100019. [CrossRef]
37. Gu, X.; Nie, W.; Li, Q.; Geng, J.; Zhou, T.; Yuan, C. Discrete Element Simulation of the Road Slope Considering Rainfall Infiltration. *Water* **2022**, *14*, 3663. [CrossRef]